Aberystwyth University

Repeat UAV photogrammetry to assess calving front dynamics at a large outlet glacier draining the Greenland Ice Sheet

Ryan, J. C.; Hubbard, A. L.; Todd, J.; Carr, J. R.; Box, J. E.; Christoffersen, P.; Holt, T. O.; Snooke, N.

The Cryosphere
Discussions

Open Access

Repeat UAV photogrammetry to assess calving front dynamics at a large outlet glacier draining the Greenland Ice Sheet

J. C. Ryan[1], A. L. Hubbard[1], J. Todd[2], J. R. Carr[1], J. E. Box[3], P. Christoffersen[2], T. O. Holt[1], and N. Snooke[4]

[1]Centre for Glaciology, Institute of Geography and Earth Sciences, Aberystwyth University, Aberystwyth, SY23 3DB, UK
[2]Scott Polar Research Institute, University of Cambridge, Cambridge, UK
[3]Geological Survey of Denmark and Greenland, Copenhagen, Denmark
[4]Department of Computer Science, Aberystwyth University, Aberystwyth, SY23 3DB, UK

Correspondence to: J. C. Ryan (jor44@aber.ac.uk) and N. Snooke (nns@aber.ac.uk)

TCD

8, 2243–2275, 2014

Repeat UAV photogrammetry to assess calving front dynamics

J. C. Ryan et al.

Title Page

Abstract | Introduction

Conclusions | References

Tables | Figures

◀ | ▶

◀ | ▶

Back | Close

Full Screen / Esc

Printer-friendly Version

Interactive Discussion

Abstract

To quantify the ice-ocean processes which drive dynamic and geometric change at calving outlet glaciers, detailed measurements beyond the capability of present satellites are required. This study presents the application of a cost-effective ($< \text{USD}\,2000$),
unmanned aerial vehicle (UAV) to investigate frontal dynamics at a major outlet draining the western sector of the Greenland Ice Sheet. The UAV was flown over Store Glacier on three sorties during summer 2013 and acquired over 2000 overlapping, geo-tagged images of the calving front at $\sim 40\,\text{cm}$ resolution. Stereo-photogrammetry applied to these images enabled the extraction of high-resolution digital elevation models with an
accuracy of $\pm 1.9\,\text{m}$ which we used to quantify glaciological processes from early July to August 2013. The central zone of the calving front advanced by $\sim 500\,\text{m}$ whilst the lateral margins remained stable. In addition, the ice surface thinned by $3.5\,\text{m}\,\text{m}^{-1}$during the melt-season in association with dynamic thinning. Ice flux through the calving front is calculated at $2.96 \times 10^7\,\text{m}^3\,\text{d}^{-1}$, equivalent to 11 Gta^{-1}, which is compara-
ble to flux-gate estimates of Store Glacier's annual discharge. Water-filled crevasses were observed throughout the observation period, but covered a limited area (1200 to $12\,000\,\text{m}^2$ of the $\sim 5 \times 10^6\,\text{m}^2$ surveyed area) and did not appear to exert any significant control over calving. We conclude that the use of repeat UAV surveys coupled with the processing techniques outlined in this paper have a number of important potential
applications to tidewater outlet glaciers.

1 Introduction

Observational and modelling studies have demonstrated that Greenland's marine outlet glaciers have a complex and potentially non-linear response to both environmental forcing (e.g. Vieli et al., 2001; Benn et al., 2007; Holland et al., 2007; Howat et al.,
2010; Hubbard, 2011; Joughin et al., 2012; Walter et al., 2012; Carr et al., 2013) and to changes in front position (Howat et al., 2007; Luckman et al., 2006; Joughin, 2008).

J. C. Ryan et al.

To quantify these processes and feedbacks, regular and accurate high-resolution measurements are required to capture the key spatio-temporal linkages between rates of ice calving, flow, surface lowering and frontal advance/retreat. Despite significant advances in satellite remote-sensing, limitations of spatial resolution (e.g. MODIS) and/or frequency of repeat imagery (e.g. Landsat or TSX) renders detailed, day-to-day analysis of calving front dynamics impossible. On the other hand, acquisition of digital imagery from UAVs combined with the development of stereo-photogrammetry software has enabled the provision of high-resolution, 3D geo-referenced data on demand for geo-science applications (e.g. d'Oleire-Oltmanns et al., 2012; Hugenholtz et al., 2012, 2013; Lucieer et al., 2014). This represents an effective, low-cost technique for acquiring aerial data in remote, hazardous and/or inaccessible regions and recent applications for emerging snow and ice investigation abound the web (for example, see the highly informative site of Matt Nolan (http://www.drmattnolan.org/photography/2013/)). To date, published (peer-reviewed) application appears to be limited to the investigation of inter-annual changes of a land-terminating glacier on Bylot Island, Canadian Arctic (Whitehead et al., 2013).

Between July and August 2013, an off-the-shelf, fixed wing UAV equipped with a compact digital camera flew three sorties over the calving front of Store Glacier, West Greenland. The aerial photographs obtained during these flights were used to produce high-resolution (~ 40 cm) (Table 1) digital elevation models (DEMs) and orthophotos of the glacier terminus. These data allowed the investigation of the spatially complex and time-varying glaciological processes operating at the glacier's calving front. The aim of this paper is to:

1. Detail the UAV, in terms of its payload and camera settings, and its specific deployment to Store Glacier.

2. Describe the techniques used for processing the aerial images and quantifying glaciological processes.

3. Discuss the significance of the data we obtained which includes calving events, the character, orientation and morphology of crevasses, surface velocities, ice discharge and changes in thickness and position of the calving front.

2 Data and methods

2.1 Study site

Store Glacier is a large marine-terminating (tidewater) outlet glacier located in the Uummannaq District of West Greenland (Fig. 1). The calving front has a width of 5.3 km and an aerial calving front (freeboard) of up to 110 m a.s.l. (Ahn and Box, 2010). Aerial photography from 1948 reveals that Store Glacier's frontal position has remained stable over the last 65 years (Weidick, 1995) although seasonally, the calving front experiences advance and retreat of up to 400 m (Howat et al., 2010). These fluctuations appear to coincide with the winter formation and spring break-out of the sea-ice mélange: a rigid conglomeration of calved ice and sea ice locally referred to as sikussak. The break-down and loss of rigidity of the ice mélange with increased air temperature from May to June coincides with a synchronous 14 and 30 % increase in velocity near the calving front suggesting that the mélange directly buttresses flow in winter and spring (Ahn and Box, 2010; Walter et al., 2012). After the ice mélange breaks-out completely, Walter et al. (2012) observed diurnal changes in surface velocity that appear to correspond to tidal fluctuations. This study focuses specifically on glacier dynamics during the melt season under open-water, tidal modulation of ice flow.

2.2 UAV platform

The UAV airframe is an off-the-self "Skywalker X8" (www.hobbyking.com) which has wing-span of 2120 cm and is made from EPP foam (Fig. 2). For this deployment, the X8 was powered by two 5Ah 4-cell (14.8 V) Lithium Polymer batteries driving a 910 W brushless electric motor turning an 11 × 7 foldable propeller. In this configuration, the

X8 has a flying mass of ∼ 3 kg (including 0.7 kg payload), which allows a cruising speed of around 55–70 km per hour with a maximum range of ∼ 60 km in relatively calm conditions at constant altitude. Larger propeller, motor and battery configurations would further improve the endurance and range of the X8 UAV but for this study, a small

5   propeller/high-rev motor combination was chosen to provide maximum instantaneous thrust to ensure a clean launch (for novice operators) and to handle the potentially strong katabatic-winds encountered during its 40 km sortie.

    The autopilot is an open-source project called "Ardupilot" (http://ardupilot.com/) based on a Atmel 2560 8bit microcontroller and standard radio-control parts includ-

10   ing 2.4 GHz radio control and pulse-width modulation (PWM) controlled servos for aileron and elevon control (Fig. 2). Ardupilot implements a dual-level proportional-integral-derivative (PID) controller architecture. The lower-level controls flight stabilisation and the higher-level controls based navigation. Tuning of the PID parameters is necessary to suit the mass and dynamics of the airframe to ensure accurate stabili-

15   sation without pitch/roll oscillation (lower level controller) or flight path weaving (higher level controller). The autopilot allows the UAV to fly autonomously according to a pre-programmed flight path defined by a series of waypoints chosen by the user. The autopilot utilises a GPS for navigation, a triple axis accelerometer and gyro for stabilisation, and a barometric pressure sensor for altitude control and these parameters are

20   logged to memory at 10 Hz throughout the flight (Fig. 2).

    The advantage of this package is that it can be assembled within a day from off-the-shelf parts and is cost-effective at less than USD 2000. The X8 is also relatively straightforward to fly, robust, easily repairable and floats; all added bonuses when being deployed in remote areas by relative novices. Furthermore, the Ardupilot firmware is

25   open source and hence can be programmed for specific requirements, for example camera triggering (see below).

    Two light-weight digital cameras were trialled at the field-site: a Panasonic Lumix DMC-LX5 10.1 megapixel (MP) camera with a 24 mm wide-angle zoom lens and a 16.1 MP Sony NEX-5N with a 16 mm fixed focal-length lens though results presented here

are limited to the former. A SPOT GPS tracking device was also included in the payload to facilitate recovery should a mission fail (which it did). The focal length of the Lumix lens was adjusted to 5.1 mm (35 mm equivalent) to allow the widest possible coverage which gave the camera a 73.7° horizontal and 53.1° vertical field of view. A short ex-
5   posure time of 1/1600 and a focal ratio of 8 were chosen to prevent overexposure and blurring of the ice surface. The Ardupilot open-source code was amended to trigger the camera automatically at user defined time or distance intervals at or between certain waypoints. The cameras were mounted pointing downwards within the X8 airframe us-ing neoprene and velcro straps to dampen vibration in a custom recessed aperture cut
10   in the bottom with a UV filter to protect the lens and seal it.

2.3   Flight planning

Flight planning was carried out using the open-source software, APM Mission Planner (http://plane.ardupilot.com/) in conjunction with the 30 m Greenland Mapping Project (GIMP) DEM (Howat et al., 2014). To optimise spatial coverage against required res-
15   olution, flight endurance and stability, the UAV was programmed to fly at a constant altitude of 500 m a.s.l. (Fig. 1). Based on the camera's focal length and field of view (53.1° by 73.7°) the ground (sea-level) footprint at 500 m a.s.l. for each photo was ∼ 450 m × 750 m. To ensure coverage of the entire glacier terminus and overlap for successful photogrammetric processing, the four transects broadly parallel to the calv-
20   ing front were flown with ∼ 250 m separation yielding a side overlap between photos of 70 % (Fig. 1). The mean ground speed of the UAV was ∼ 70 km h^{-1} and camera trigger interval was adjusted between surveys. On flights 1 and 2, the interval between camera triggers was 1.5 s corresponding to a forward overlap of 94 % and over 1000 geo-tagged images acquired. Flight 3 had a 2.4 s interval yielding a 90 % forward over-
25   lap and 567 images (Table 1).
UAV operations were based out of a field-camp with the advantage of a 50 m area of flat alluvial terrace with relatively boulder/bedrock free ground for manual remote-control take-off and landing. This location did, however, require a ∼ 20 km transit back

and fore to the calving front over a 450 m high peninsula which significantly reduced the useful endurance over the target. Of the six sorties flown over outlet glaciers in the region during July and August 2013, the three over Store Glacier were most successful. Each sortie was 40 km long and ∼ 35 min duration after the UAV had attained
5   its operating altitude at the start of the mission and was passed from manual remote-control mode into autopilot mode (Fig. 1). Visual and remote-control contact is lost within a few km of the UAV being placed in autopilot mode hence it is worth having the 3-D waypoints and mission plan independently checked.

2.4   Three-dimensional model generation

10   Three-dimensional data were extracted from the aerial photos using Agisoft Photoscan Pro software (http://www.agisoft.ru/products/photoscan). This software's strength lies in its ability to fully automate workflow and enables non-specialists to process aerial images and produce 3-D models which can be exported as georeferenced orthophotos and DEMs (e.g. Figs. 3 and 6). The first stage of processing is image alignment
15   using the structure-from-motion (SFM) technique. SFM allows the reconstruction of 3-D geometry and camera position from a sequence of two-dimensional images captured from multiple viewpoints (Ullman, 1979). Photoscan implements SFM algorithms to monitor the movement of features through a sequence of multiple images and is used to estimate the location of high contrast features (e.g. edges), obtain the relative
20   location of the acquisition positions and produce a sparse 3-D point cloud of those features. The Ardupilot flight logs of the on-board navigation sensors allow the camera positions and the 3-D point cloud to be georeferenced within instrument precision. SFM also enables the camera calibration parameters (e.g. focal length and distortion coefficients) to be automatically refined hence there is no need to pre-calibrate the cameras
25   and lens optics (Verhoeven, 2011).

Once the photos have been aligned, a multiview reconstruction algorithm is applied to produce a 3-D polygon mesh which operates on pixel values rather than features and enables the fine details of the 3-D geometry to be constructed (Verhoeven, 2011).

Repeat UAV photogrammetry to assess calving front dynamics

J. C. Ryan et al.

The user determines the precision of the final 3-D model based on image resolution and pixel footprint. A medium quality setting was chosen yielding DEMs with between 38–40 cm pixel^{-1} resolution which were resampled to a Cartesian 50 cm grid to enable inter-comparison (Table 1). Higher resolutions (< 30 cm) are attainable but the increase in computational time and the accuracy of geo-referencing limits the benefits of such apparent precision.

Two problems of accuracy were encountered in DEM production. The first was that Photoscan failed to reconstruct a flat sea-level of constant elevation. The second was that the relative positional errors between the DEMs constructed from different sorties were up to 15 m. Positional errors were due to the specified limits of the on-board L1 GPS of ±5.0 m horizontally and, when combined with the barometric sensor, to a similar accuracy vertically. Hence, a secondary stage of processing was carried out which involved 3-D co-registration of the DEMs. To do this, the horizontal and vertical coordinates of common control points (CPs) based on distinct features like cliff bases, large boulders and promontories were extracted from the georeferenced orthoimages. The CPs that were at sea-level were nominally given elevation values of zero, re-imported into Photoscan and subsequently reprocessed along with a geodetic-GPS ground CP located at 70.401° N, −50.6654° E and 335.85 m altitude on the bedrock headland overlooking the glacier's northern flank. This procedure reduced the relative horizontal errors between the three DEMs to < 1 m and gave a flat sea-level across the glacier front with a vertical error at the known (GPS) CP of 1.4 m. After processing, the georeferenced 3-D DEMs and orthophotos were exported at 50 cm resolution for further analysis in ArcGIS and ENVI software packages.

2.5 Analysis

Changes in calving front positions were obtained from these data combined with a Landsat 8 panchromatic image obtained on 12 June (Fig. 3b). Each calving front position was digitized according to the procedure outlined by Moon and Joughin (2008) whereby a polygon of the calving front retreat or advance is digitized and divided by the

width of the glacier. This method has been used in previous studies (e.g. Howat et al., 2010; Schild and Hamilton, 2013) and enables inter-comparison of results. Surface elevation change was calculated from the residual difference of the DEMs (Fig. 3a).

Ice flow across the terminus region was calculated by feature tracking performed on successive orthophotos using the ENVI Cosi-CORR software module (Fig. 4b). These velocities were then used to estimate ice flux through the calving front for the same period under the assumption of plug flow (uniform velocity profile with depth) and using an calving front cross-section obtained from single-beam echo-sounder bathymetry across the calving front obtained by boat in 2010 and 2012. The frontal cross-section was divided into 10 m vertical strips and each one assigned a horizontal velocity value (Fig. 4a). The floatation depth and buoyancy ratio across the calving front was calculated using the ice surface (freeboard) elevation and total ice thickness with a value for the density of ice of $917\,kg\,m^{-3}$ for sea-water of $1028\,kg\,m^{-3}$ (Fig. 5a) following Motyka et al. (2011).

To investigate the distribution and patterns of crevassing, each DEM was Gaussian filtered at 200 pixels (100 m) in ArcGIS and subtracted from the original DEM to yield the pattern of negative surface anomalies. These anomalies were converted into polygons to map and hence quantify crevasse distribution and character (Fig. 6a). The resulting polygons were enclosed by a minimum bounding rectangle, which allowed the orientation, width, length and depth of crevasses to be extracted (Fig. 6a, Table 2). Water-filled crevasses were automatically located in the ENVI package using the supervised maximum likelihood classification (MLC) method. Representative training samples for water-filled areas were chosen from the colour composite orthophoto (Fig. 6b). The trained tool then classifies pixels that are interpreted as water into the desired class. The resulting raster image was converted into an ArcINFO shapefile and used to mask and define the area of the water-filled crevasses across the terminus. These procedures allow thousands of crevasses in multiple orthoimages and DEMs to be quantified easily without the difficulties and dangers associated with direct field measurements.

Title Page

Abstract | Introduction

Conclusions | References

Tables | Figures

◀ | ▶|

◀ | ▶

Back | Close

Full Screen / Esc

Printer-friendly Version

Interactive Discussion

2.6 Uncertainties and limitations

The relative horizontal uncertainties between the DEMs were investigated by feature tracking the stationary bedrock at the sides of the glacier. The RMS horizontal displacement was ±1.0 m which provides us with an approximate error estimate. The relative vertical uncertainties between the DEMs were estimated by calculating elevation differences between bedrock areas, which reveal an error estimate was ±1.9 m. Just one conventional (GPS) CP was utilised for this study; several such CPs on the bedrock either side of the glacier front would further reduce these uncertainties. A telemetric differential GPS deployed on or near the calving front, which is sufficiently large/bright to identify within the aerial imagery would allow further ground control in the centre of DEMs, away from bedrock CPs.

Due to the lack of reflected light from deep crevasse recesses, the DEM generation process cannot quantify the narrowest sections of all fractures and resultant crevasse depths are therefore a minimum estimate. The technique is also clearly limited to line of sight precluding narrow fractures which extend for tens of centimetres horizontally and potentially up to a few metres vertically (Hambrey and Lawson, 2000; Mottram and Benn, 2009).

Finally, there are a number of practical difficulties when operating an autonomous aircraft over such ranges in remote and inaccessible environments. Mission planning is critical; knowledge of the local weather conditions, as well as up-to-date satellite imagery and DEMs are a prerequisite for a successful outcome.

3 Results

Three successful UAV sorties were flown over Store Glacier calving front providing imagery, orthophotos and DEMs on the 1 and 2 July and the 23 August, herein referred to flights and associated products 1 to 3, respectively (Table 1). The interval between flights 1 and 2 was 19 h and comparison between these outputs enables identifica-

tion of processes operating over a daily (short) time-scale, be it a very specific snap-shot. The third sortie was flown 52 days later and comparison between these outputs enables investigation of late-seasonal change. The four transects flown captured just over 1 km of Store Glacier from its calving front and herein, "the terminus" refers to this section of the glacier.

3.1 Short timescale calving and surface elevation change

Residual elevation change between 1 and 2 July (Fig. 3a) reveals that the front re-treated in two sections by up to 50 and 80 m respectively. Calving event A resulted in a 450 m wide section of the terminus retreating by between 20 and 50 m, whilst event B produced between 20 m and 80 m of retreat across a 400 m section (Fig. 3a). In ad-dition to these two calving events (which are discussed in Sect. 3.6), the central 4.5 km frontal section advanced between 12 m to 16 m (Fig. 3a). At its lateral margins, the calving front shows no discernible systematic change though there are isolated, small calving events, for example, within 50 m of the southern flank (Fig. 3a). Upstream of the calving front, there is no net change in mean surface elevation away from the front and the dappled pattern of residual elevation change is a result of the advection of crevasses and seracs. Successive long profiles of the terminus between the 1 and 2 July reveal specific down-glacier crevasse advection with flow (Fig. 6) at a rate of 5 and 16 m d^{-1} on Profile 1 and 2, respectively. These results provide estimations of surface velocities which are confirmed by feature tracking in the Sect. 3.4.

3.2 Seasonal timescale calving front position and surface elevation change

As could be expected, over the entire melt-season, larger fluctuations in calving front position are observed (Fig. 3b). Over the 19 day period from 12 June to 1 July, mean frontal retreat was 160 m (Fig. 3c) and between 2 July and 23 August, the calving front advanced by an average of ∼ 110 m to a position similar to that in 12 June (Fig. 3d). These mean values, however, do not convey the full extent and detail of the changes

observed in the calving front. For example, the central section of the calving front re-treated by up to 525 m between the 12 June and 1 July and advanced by up to 450 m between the 2 July and 23 August (Fig. 3b). Furthermore, the lateral margins of Store Glacier (the southern 850 m and the northern 1.5 km) are relatively stable with < 50 m change in position. Over the 52 day period between the 2 July (Flight 2) and 23 August (Flight 3) widespread surface lowering of 6.1 ± 1.9 m (or 3.5 m m^{-1}) was observed across Store Glacier terminus (Fig. 4a), significantly larger than the estimated vertical uncertainties of the DEMs. Despite the same dappled patterns caused by local ad-vection of crevasses and seracs, there is significant lowering possibly attributable to dynamic thinning occurring across the terminus extending to at least 1 km up-glacier beyond the survey area.

3.3 Bathymetry

The deepest sector of the calving front is located 1 km south of the centreline and exceeds 540 m below sea level (Fig. 5a). This 200 m sector also corresponds to the greatest thickness of ~ 600 m. To the south of this deepest point, the bottom rises rapidly to a 200 m deep shelf located 500 m from the flank. To the north of the deep-est point, the bottom shallows more gently to within 400 m where it becomes steeper towards the fjord wall.

3.4 Surface velocities

The spatial pattern of surface flow from feature tracking of images between the 1 and 2 July varies considerably across the terminus of Store Glacier (Fig. 4b) attaining ve-locities of 16 m d^{-1} (5.8 km a^{-1}) near the centre of the glacier down to 2.5 m d^{-1} at the lateral flanks. Surface velocities are related to slope, depth, thickness and distance from the lateral margins (Fig. 5c and d). As would be expected, maximum velocities (> 14 m d^{-1}) correlate roughly with maximum depth and towards the north flank are lin-early correlated ($R^2 = 0.90$) with frontal depth (Fig. 5c). Towards the southern flank the

relationship is less apparent especially between 200 to 350 m. There is a strong correlation between velocities and distance from the lateral margins which can be approximated by a power function ($R^2 = 0.90$) (Fig. 5d). Although application of the floatation criteria indicates that parts of calving front are buoyant (Fig. 5a), side-scan sonar observations reveal that the glacier front rests on the bottom. When the surface flow pattern is combined with frontal bathymetric data we estimated that the mass flux through the calving front of Store Glacier was $2.96 \times 10^7 \, \mathrm{m}^3 \, \mathrm{d}^{-1}$, equivalent to $\sim 11 \, \mathrm{Gt} \, \mathrm{a}^{-1}$.

Seasonal flow patterns were not obtainable between 2 July and 23 August as the majority of any matching features within the study area required for tracking had already calved into the ocean. Furthermore, it is likely that the morphology of many crevasses and seracs will have changed significantly through melt and deformation and would not be recognised by the cross-correlation procedure.

3.5 Crevassing

The morphology and orientation of crevasses varies markedly across the terminus (Fig. 6). The largest crevasses occur in a sector south of the glacier centre line in zone 4 (Fig. 6, Table 2). Here, crevasses have mean minimum depths of 18 m, lengths of 68 m and widths of 31 m. The largest crevasses are up to 30 m deep, over 500 m long and nearly 200 m wide but no crevasses that penetrated below sea-level were identified. Most crevasses in this region are arcuate with limbs pointing towards the calving front and are orientated obliquely to the direction of ice flow (Fig. 6). This arcuate morphology of crevasses continues across the central 3 km of the terminus in zone 3 (Fig. 6). Here, crevasses have mean a depth of 10.5 m, length of 50 m and widths of 18 m (Table 2). In zone 2, 300 to 500 m from the northern flank crevasses are aligned obliquely to the direction of ice flow (30–45°). Up to the fjord walls in zones 1 and 5, crevasses are generally orientated parallel to the ice flow (< 15°) (Fig. 6, Table 2) and are much smaller with a mean lengths of 22 m and widths of 8 m (Table 2). No discernible difference in average crevasse depths, lengths or widths was observed

between the early July and late August and the pattern and character of crevassing was very similar.

Water-filled crevasses were clustered in zone 4, coinciding with the sector of larger crevasses (Fig. 6b). Water-filled crevasses covered $12\,000\,\text{m}^2$ or 0.24 % of the survey area (to ~ 1 km from the calving front) (Table 1) on 2 July. Some 42 individual water-filled crevasses were identified with the largest having an area of $1200\,\text{m}^2$. By 23 August, the number, size and total area of water filled crevasses were lower: only 10 water-filled crevasses could be identified, the largest of which was $400\,\text{m}^2$ and with a total area of $1230\,\text{m}^2$ (0.025 % of the survey area). We were not able to ascertain the depth of water in the crevasses as no crevasses could be identified which drained or filled between observations but this would be a specific aim of future studies which, with regular sorties, could potentially measure the depth of a crevasse before filling or after drainage or otherwise exploit light reflectance relationship with water depth.

Successive profiles of the terminus from 1 and 2 July demonstrate how the UAV surveys are capable of capturing the displacement of crevasses, which advect downstream at a rate of 5 and $16\,\text{m}\,\text{d}^{-1}$ in Profiles 1 and 2, respectively (Fig. 6). The techniques used in this study are therefore capable of identifying changes in crevasses geometry, particularly width and depth through time.

3.6 Calving events

The two calving events identified between 1 and 2 July appear to take place under contrasting conditions. Event A consisted of the calving of multiple, relatively small ice blocks with the glacier failing along two main crevasses located 30 and 50 m behind the calving front. These crevasses were between 8 and 10 m deep, respectively and in this instance, the crevasses located closest to the front were the ones that failed. Event B appears to be a single large event caused by the fracturing of a series of parallel crevasses which were up to 14 m deep and 60 m behind the calving front. Unlike, calving event A, the crevasses that failed in event B were not the closest to the calving front. Indeed, there were other crevasses that were deeper and located nearer

to the front, yet did not calve. Water was not observed in any of the crevasses along which calving took place.

4 Discussion

4.1 Changes occurring over a daily timescale

The daily surface flow velocities obtained between 1 and 2 July 2013 (up to $16\,\mathrm{m\,d^{-1}}$) are consistent with results obtained in previous studies using other techniques, such as feature tracking images from a land-based time-lapse camera (between 11 and $15\,\mathrm{m\,d^{-1}}$) (Ahn and Box, 2010; Walter et al., 2012). Speckle-tracking of successive TerraSAR-X images reveals that the July monthly average flow velocities at the terminus of the glacier was between 18.3 and $18.9\,\mathrm{m\,d^{-1}}$ in 2009 and 2011, respectively (Joughin et al., 2010). Store Glacier therefore appears to be flowing between 7 and 26 % slower between the 1 and 2 July than the monthly average suggesting that either (1) velocity fluctuations on daily timescales vary considerably and average out over the month, or, that (2) the daily mean flow across the terminus does not vary and hence was significantly less in 2013 than 2009 and 2011. Evidence from other tidewater glaciers favours the first hypothesis because velocity fluctuations of 17–38 % between mid-June and late-September have been reported for major West Greenland tidewater glaciers including accelerations of 15–18 % after large calving events which lasted between 6 and 10 days (Ahn and Box, 2010). However, the second hypothesis cannot be dismissed as surface melt was much retarded in July 2013 compared to previous years.

The orientation of crevasses suggests that lateral drag is an important resistive stress on Store Glacier. The lateral margins of the Store are characterised by crevasses that are orientated parallel to the direction of flow which suggests that they have formed in response to simple shear stresses associated with the drag of the fjord walls (Fig. 6) (Benn and Evans, 2010). The importance of lateral drag is further demonstrated by the

Title Page

Abstract | Introduction

Conclusions | References

Tables | Figures

|◄ | ►|

◄ | ►

Back | Close

Full Screen / Esc

Printer-friendly Version

Interactive Discussion

morphology of crevasses found near the glacier flowline (Fig. 6). Their arcuate nature indicates that the principal tensile stresses operating on the ice have been rotated by lateral gradients in ice velocity. These gradients are caused by the simple shear stress between the fjord walls and the margins of the glacier which cause the ice to flow slower (Fig. 4b) (Benn and Evans, 2010).

The simple shearing caused by velocity gradients is further demonstrated by the differing relationship between velocity and depths between the north and south side of the glacier (Fig. 5c and d). On the north side, the velocity increases gradually from the fjord wall to the centre of the glacier, reflecting the gradual deepening of bathymetry and the resulting decrease of basal and lateral drag. On the south side, the velocities are higher than the north side for given depths and distances from the lateral margins (Fig. 5c and d). We hypothesize that, because the deepest part of the glacier is situated 1 km south of the centreline, the ice on south side is more influenced by faster flowing ice which exerts a simple shear stress on the shallower, adjacent ice (250–400 m thick). This causes the shallow ice to flow faster than ice with similar thicknesses and distance from the lateral margins on the north side (Fig. 5c).

The mass flux through the calving front was calculated at $2.96 \times 10^7\,\mathrm{m^3\,d^{-1}}$ which needs to be balanced by three main frontal processes: calving, submarine melting and advective advance. Both calving and advance were observed in this study but it is likely that submarine melting also has a large role in ice output at a daily timescale. For example, Xu et al. (2013) used oceanographic data to calculate a melt water flux of between 0.5 and $1.1 \times 10^7\,\mathrm{m^3\,d^{-1}}$ from Store Glacier in August 2010 equivalent to 17–37 % of the mass flux calculated in by our study. For comparison, Rink glacier has an ice flux of $3.0 \times 10^7\,\mathrm{m^3\,d^{-1}}$ of which 27 % is estimated to be lost through submarine melting each day (Enderlin and Howat, 2013).

4.2 Changes occurring over a seasonal timescale

The observed seasonal retreat of Store Glacier (160 m between June and July) is of the order of the mean seasonal retreat observed during the same months between

Title Page

Abstract | Introduction

Conclusions | References

Tables | Figures

|◀ | ▶|

◀ | ▶

Back | Close

Full Screen / Esc

Printer-friendly Version

Interactive Discussion

2000 and 2009 (Howat et al., 2010). Other tidewater glaciers in Greenland have similar melt-season retreat patterns (e.g. Howat et al., 2010) though the magnitude of retreat displayed by Store Glacier is much less than other glaciers (Schild and Hamilton, 2013). For example, Rink Glacier, which is also situated in the Uummannaq Bay, has a mean seasonal retreat of 960 m between 2001 and 2010.

The lack of variation in the position of the lateral margins of the glacier shows that a balance is maintained between the ice flux input and submarine melting and calving output in this zone throughout the melt season. The balance could be explained by the mechanism of calving events. At the lateral margins calving is characterised by small, regular events such as calving event A (Fig. 3a). The regularity of these small events means that any small advance or retreat is regulated almost instantly by changes in calving rate which returns the lateral margins of the glacier to the same position. Calving rate could also be moderated by changes in the bathymetry. When the lateral margins advance, calving rates increase due to the abrupt deepening of the bathymetry seaward of the lateral margins of the glacier which cause basal drag to be reduced. Ice flow acceleration can lead to increased longitudinal stretching and deeper crevassing, thereby increasing calving rate and leading to retreat to its original, bathymetrically-pinned position.

The centre of the calving front is much more active with calving and submarine melt rates that vary on a seasonal timescale. We propose that the main cause of variability is due to calving rates which are highly irregular throughout the melt season (Jung et al., 2010). Our observations also support the suggestion that calving rates are dominated by major calving events which have a time interval of around 28 days (e.g. Jung et al., 2010). If the calving front advances for 28 days at $16\,\mathrm{m\,d^{-1}}$, it will advance 448 m. A large, single calving event can then cause a retreat of ~ 448 m and which would explain the variation in the position of the calving front during the melt season (Fig. 3b). On 25 August 2013, a tabular iceberg with a length of ~ 500 m was observed to calve from the central zone of Store Glacier.

Towards the end of the melt-season (23 August), widespread surface lowering is observed (Fig. 4a). The lowering of $3.5\,\mathrm{m\,m^{-1}}$ is likely a dynamic response to flow acceleration as surface ablation alone cannot account for the magnitude of observed thinning. For example, Enderlin and Howat (2013) calculated mean surface melt rates of $\sim 0.001\,\mathrm{m\,d^{-1}}$ at the terminus of Rink Glacier during the summer (June–August) between 2000 and 2010. Acceleration of ice flow on the other hand is well-documented. According to Ahn and Box (2010), flow velocity of Store Glacier increases between 14 and 30 % after the clearing of the ice mélange in mid- to late-May. Furthermore, large calving events also initiate flow acceleration of 15–18 % (Ahn and Box, 2010). These changes may well promote seasonally induced dynamic thinning across the terminus region of Store Glacier. The thinning is important as it brings the glacier closer to floatation and reduces basal drag (Vieli et al., 2001; Pfeffer, 2007). Unfortunately, feature tracking could not be performed between 2 July and 23 August, so the impact of seasonal thinning on flow velocities is uncertain. A minimum repeat survey frequency would preclude these feature tracking issues.

Another important observation is the order of magnitude reduction of the area of water-filled crevasses between early July and late August (Fig. 6). The extent of water-filled crevasses is likely influenced by the effect of surface meltwater production from air temperatures. Air temperatures were recorded 4 m a.s.l. at a weather station located near the UAV launch site (Fig. 1). These data reveal that day-time temperatures rose to 14 °C and were no lower than 3 °C on the four days prior to the UAV sortie on the 2 July. In contrast, night-time temperatures dropped to less than 1 °C and day-time temperature were no higher than 5 °C on the four consecutive days prior to the UAV sortie on the 23 August. These data signify a potential mechanism by which increased air temperatures could increase calving rate and cause changes to the ice dynamics (Benn et al., 2007). Water-filled crevasses are hypothesized to penetrate deeper than crevasses without water (Weertman, 1973; Van der Veen, 1998; Benn et al., 2007) and hence act as foci for calving. The calving events observed in this study did not involve any water-filled crevasses. It remains to be seen whether water-filled crevasses

Repeat UAV photogrammetry to assess calving front dynamics

J. C. Ryan et al.

Title Page

Abstract	Introduction
Conclusions	References
Tables	Figures

◀ | ▶|

◀ | ▶

Back | Close

Full Screen / Esc

Printer-friendly Version

Interactive Discussion

have an impact on calving from Store Glacier but our limited results do not support this hypothesis.

5 Conclusions and future directions

A UAV equipped with a commercial digital camera enabled us to obtain high resolution DEMs and orthophotos of the calving front of a major tidewater glacier at an affordable price. Airborne LiDAR currently presents the only alternative method for acquiring DEMs with comparable accuracy and precision. However, to fly consecutive sorties in a remote environment would be far more expensive and with sufficient ground control points the digital photogrammetry approach may exceed the accuracy of this technique.

The three sorties flown enabled key glaciological parameters to be quantified at sufficient detail to reveal that the terminus of Store Glacier is a complex system with large variations in crevasse patterns surface velocities, calving processes, surface elevations and front positions at a daily and seasonal timescale. Surface velocities vary across the terminus and are influenced by both basal and lateral drag (Fig. 4b, 5c, d). The oblique orientation and arcuate nature of crevasses suggests that the principal extending strain rate is orientated obliquely to the direction of flow and we therefore propose that resistive stresses at the terminus of Store Glacier are dominated by lateral drag (Fig. 6). With this in mind, the retreat of Store into a wider fjord could significantly increase the ice discharge. We estimated that the current ice flux of Store was $2.96 \times 10^7 \, \text{m}^3$ and observed a small terminus advance between 1 and 2 July (Fig. 3a, 5a). This advance shows that, during this period, the sum of calving and submarine melt rates are less than the ice flux. Calving is, however, an irregular process and the fact that the position of the calving front returned to its 12 June position by 23 August suggests that, over this timescale, calving and submarine melt rate balance ice flux (Fig. 3B). Late-season dynamic thinning of $3.5 \, \text{m} \, \text{m}^{-1}$ is likely a result of increased flow velocities after the removal of the ice mélange which can increase flow velocities by 14–30 % (Fig. 4a) (Ahn and Box, 2010). Water-filled crevasses covered 0.24 % of the survey area on 2 July

but this fell to 0.025 % on 23 August (Fig. 6). It remains to be seen whether water-filled creases are more likely to initiate calving events but these data signify a potential mechanism by which increased air temperatures could increase calving rate and impact on ice dynamics.

Future studies, with a larger number of sorties could be used to compare and investigate further glaciological changes over a more continuous timespan. There is also the possibility of a more varied payload with radiation, albedo and other fine-band sensors as well as a laser altimeter for constant height above ground surveys. Therefore there are many potential cryospheric applications for investigation of sea-ice, outlet glacier and ice masses that can be achieved with the use of repeat UAV surveys. For marine-terminating outlet glaciers, a UAV carrying a digital camera would be sufficient to investigate the following projects:

– Analysis of the thickness and back-stress exerted by the ice mélange during the winter and the effect of its break-up on outlet glacier flow, calving rate and character.

– Seasonal changes in the depth, density, orientation and nature of crevassing and their impact on calving rate and character.

– The influence of daily to seasonal melt and supraglacial lake drainage on downstream dynamics and calving.

– Analysis of daily to seasonal fluctuations in terminus position and impact on up-glacier flow.

– Determination of bulk frontal discharge and associated thinning throughout the season.

Full Screen / Esc

Printer-friendly Version

Interactive Discussion

References

AgiSoft LLC: AgiSoft PhotoScan, available at: http://www.agisoft.ru/products/photoscan/ (last access: 14 February 2014), 2013.

Ahn, Y. and Box, J. E.: Glacier velocities from time-lapse photos: technique development and first results from the Extreme Ice Survey (EIS) in Greenland, J. Glaciol., 56, 723–734, doi:10.3189/002214310793146313, 2010.

Benn, D. I. and Evans, D. J. A.: Glaciers and Glaciation, Hodder Education, London, 2010.

Benn, D. I., Warren, C. R., and Mottram, R. H.: Calving processes and the dynamics of calving glaciers, Earth-Sci. Rev., 82, 143–179, doi:10.1016/j.earscirev.2007.02.002, 2007.

Box, J. E. and Decker, D. T.: Greenland marine-terminating glacier area changes: 2000–2010, Ann. Glaciol., 52, 91–98, 2011.

Carr, J. R., Vieli, A., and Stokes, C. R.: Climatic, oceanic and topographic controls on marine-terminating outlet glacier behavior in north-west Greenland at seasonal to interannual timescales, J. Geophys. Res., 118, 1210–1226, 2013.

Carrivick, J. L., Smith, W. M., Quincey, D. J., and Carver, S. J.: Developments for budget remote sensing in the geosciences, Geology Today, 29, 138–143, 2013.

d'Oleire-Oltmanns, S., Marzolff, I., Peter, K. D., and Ries, J. B.: Unmanned Aerial Vehicle (UAV) for monitoring soil erosion in Morocco, Remote Sensing, 4, 3390–3416, 2012.

Enderlin, E. M. and Howat, I. M.: Submarine melt rate estimates for floating termini of Greenland outlet glaciers (2000–2010), J. Glaciol., 59, 67–75, doi:10.3189/2013jog12j049, 2013.

Hambrey, M. J. and Lawson, W.: Structural styles and deformation fields in glaciers: a review, Geol. Soc. Spec. Publ., 176, 59–83, doi:10.1144/Gsl.Sp.2000.176.01.06, 2000.

Holland, D. M., Thomas, R. H., De Young, B., Ribergaard, M. H., and Lyberth, B.: Acceleration of Jakobshavn Isbrae triggered by warm subsurface ocean waters, Nat. Geosci., 1, 659–664, doi:10.1038/Ngeo316, 2008.

Howat, I. M., Joughin, I., and Scambos, T. A.: Rapid changes in ice discharge from Greenland outlet glaciers, Science, 315, 1559–1561, doi:10.1126/science.1138478, 2007.

Howat, I. M., Box, J. E., Ahn, Y., Herrington, A., and McFadden, E. M.: Seasonal variability in the dynamics of marine-terminating outlet glaciers in Greenland, J. Glaciol., 56, 601–613, 2010.

Title Page

Abstract | Introduction

Conclusions | References

Tables | Figures

|◄ | ►|

◄ | ►

Back | Close

Full Screen / Esc

Printer-friendly Version

Interactive Discussion

Howat, I. M., Negrete, A., and Smith, B. E.: The Greenland Ice Mapping Project (GIMP) land classification and surface elevation datasets, The Cryosphere Discuss., 8, 453–478, doi:10.5194/tcd-8-453-2014, 2014.

Hubbard, A.: The Times Atlas and actual Greenland ice loss, Geology Today, 27, 214–217, 2011.

Hugenholtz, C. H., Levin, N., Barchyn, T. E., and Baddock, M. C.: Remote sensing and spatial analysis of aeolian sand dunes: a review and outlook, Earth-Sci. Rev., 111, 319–334, doi:10.1016/j.earscirev.2011.11.006, 2012.

Hugenholtz, C. H., Whitehead, K., Brown, O. W., Barchyn, T. E., Moorman, B. J., LeClair, A., Riddell, K., and Hamilton, T.: Geomorphological mapping with a small unmanned aircraft system (sUAS): feature detection and accuracy assessment of a photogrammetrically-derived digital terrain model, Geomorphology, 194, 16–24, doi:10.1016/j.geomorph.2013.03.023, 2013.

Joughin, I., Das, S. B., King, M. A., Smith, B. E., Howat, I. M., and Moon, T.: Seasonal speedup along the western flank of the Greenland ice sheet, Science, 320, 781–783, doi:10.1126/science.1153288, 2008.

Joughin, I., Smith, B. E., Howat, I. M., Scambos, T., and Moon, T.: Greenland flow variability from ice-sheet-wide velocity mapping, J. Glaciol., 56, 415–430, 2010.

Joughin, I., Smith, B. E., Howat, I. M., Floricioiu, D., Alley, R. B., Truffer, M., and Fahnestock, M.: Seasonal to decadal scale variations in the surface velocity of Jakobshavn Isbrae, Greenland: observation and model-based analysis, J. Geophys. Res.-Ea. Surf., 117, F02030, doi:10.1029/2011jf002110, 2012.

Jung, J., Box, J. E., Balog, J. D., Ahn, Y., Decker, D. T., and Hawbecker, P.: Greenland Glacier Calving Rates from Extreme Ice Survey (EIS) Time Lapse Photogrammetry, C23B-0628, American Geophysical Union, San Francisco, 2010.

Kargel, J. S., Ahlstrøm, A. P., Alley, R. B., Bamber, J. L., Benham, T. J., Box, J. E., Chen, C., Christoffersen, P., Citterio, M., Cogley, J. G., Jiskoot, H., Leonard, G. J., Morin, P., Scambos, T., Sheldon, T., and Willis, I.: Brief communication Greenland's shrinking ice cover: "fast times" but not that fast, The Cryosphere, 6, 533–537, doi:10.5194/tc-6-533-2012, 2012.

Lucieer, A., Turner, D., King, D. H., and Robinson, S. A.: Using an unmanned aerial vehicle (UAV) to capture micro-topography of Antarctic moss beds, Int. J. Appl. Earth Obs., 27, 53–62, doi:10.1016/j.jag.2013.05.011, 2014.

Title Page

Abstract | Introduction

Conclusions | References

Tables | Figures

|◄ | ►|

◄ | ►

Back | Close

Full Screen / Esc

Printer-friendly Version

Interactive Discussion

Luckman, A., Murray, T., de Lange, R., and Hanna, E.: Rapid and synchronous ice-dynamic changes in East Greenland, Geophys. Res. Lett., 33, L03503, doi:10.1029/2005GL025428, 2006.

Moon, T. and Joughin, I.: Changes in ice front position on Greenland's outlet glaciers from 1992 to 2007, J. Geophys. Res.-Ea. Surf., 113, F02022, doi:10.1029/2007jf000927, 2008.

Mottram, R. H. and Benn, D. I.: Testing crevasse-depth models: a field study at Breioamerkurjokull, Iceland, J. Glaciol., 55, 746–752, doi:10.3189/002214309789470905, 2009.

Motyka, R. J., Truffer, M., Fahnestock, M., Mortensen, J., Rysgaard, S., and Howat, I.: Submarine melting of the 1985 Jakobshavn Isbrae floating tongue and the triggering of the current retreat, J. Geophys. Res.-Ea. Surf., 116, F01007, doi:10.1029/2009jf001632, 2011.

O'Neel, S., Pfeffer, W. T., Krimmel, R., and Meier, M.: Evolving force balance at Columbia Glacier, Alaska, during its rapid retreat, J. Geophys. Res.-Ea. Surf., 110, F03012, doi:10.1029/2005jf000292, 2005.

Pfeffer, W. T.: A simple mechanism for irreversible tidewater glacier retreat, J. Geophys. Res.-Ea. Surf., 112, F03S25, doi:10.1029/2006jf000590, 2007.

Raymond, C.: Shear margins in glaciers and ice sheets, J. Glaciol., 42, 90–102, 1996.

Rignot, E., Koppes, M., and Velicogna, I.: Rapid submarine melting of the calving faces of West Greenland glaciers, Nat. Geosci., 3, 187–191, doi:10.1038/Ngeo765, 2010.

Schild, K. M. and Hamilton, G. S.: Seasonal variations of outlet glacier terminus position in Greenland, J. Glaciol., 59, 759–770, doi:10.3189/2013jog12j238, 2013.

Sundal, A. V., Shepherd, A., van den Broeke, M., Van Angelen, J., Gourmelen, N., and Park, J.: Controls on short-term variations in Greenland glacier dynamics, J. Glaciol., 59, 883–892, doi:10.3189/2013jog13j019, 2013.

Ullman, S.: The interpretation of structure from motion, P. R. Soc. London, 203, 405–426, 1979.

Verhoeven, G.: Taking computer vision aloft – archaeological three-dimensional reconstructions from aerial photographs with Photoscan, Archaeol. Prospect., 18, 67–73, 2011.

Vieli, A., Funk, M., and Blatter, H.: Tidewater glaciers: frontal flow acceleration and basal sliding, Ann. Glaciol., 31, 217–221, doi:10.3189/172756400781820417, 2000.

Xu, Y., Rignot, E., Fenty, I., Menemenlis, D., and Flexas, M. M.: Subaqueous melting of Store Glacier, West Greenland from three-dimensional, high-resolution numerical modeling and ocean observations, Geophys. Res. Lett., 40, 4648–4653, doi:10.1002/Grl.50825, 2013.

Title Page

Abstract | Introduction

Conclusions | References

Tables | Figures

|◄ | ►|

◄ | ►

Back | Close

Full Screen / Esc

Printer-friendly Version

Interactive Discussion

Walter, J. I., Box, J. E., Tulaczyk, S., Brodsky, E. E., Howat, I. M., Ahn, Y., and Brown, A.: Oceanic mechanical forcing of a marine-terminating Greenland glacier, Ann. Glaciol., 53, 181–192, doi:10.3189/2012aog60a083, 2012.

Weertman, J.: Can a water-filled crevasse reach the bottom surface of a glacier?, IAHS Publ., 95, 139–145, 1973.

Whitehead, K., Moorman, B. J., and Hugenholtz, C. H.: Brief Communication: Low-cost, on-demand aerial photogrammetry for glaciological measurement, The Cryosphere, 7, 1879–1884, doi:10.5194/tc-7-1879-2013, 2013.

Weidick, A.: Greenland, with a section on Landsat images of Greenland, in: Satellite Image Atlas of Glaciers of the World, edited by: Williams, R. S. and Ferrigno, J. G., US Geological Survey, Washington DC, C1–C105 (USGS Professional Paper 1386-C), 1995.

Table 1. Attributes of the flight surveys and image acquisition of the UAV.

Flight no.	Date	Interval between images (s)	No. images	Glacier coverage (km^2)	Resolution of DEM (cm pixel^{-1})
1	1 Jul	1.55	611	3.17	40
2	2 Jul	1.51	1051	4.95	38
3	23 Aug	2.36	567	5.02	39

Title Page

Abstract | Introduction

Conclusions | References

Tables | Figures

◀◀ | ▶▶

◀ | ▶

Back | Close

Full Screen / Esc

Printer-friendly Version

Interactive Discussion

Table 2. Attributes of mean crevasse width, length and orientation in each zone labelled in Fig. 5. Orientations are measured along the long-axis of each crevasse and are in respect to the direction of flow which is 0°.

Zone	Mean width (m)	Mean length (m)	Mean orientation (°)
Zone 1	3.6	9.4	9.2
Zone 2	4.8	14.0	36.7
Zone 3	10.5	32.6	85.1
Zone 4	6.5	17.8	60.4
Zone 5	3.5	8.5	10.8
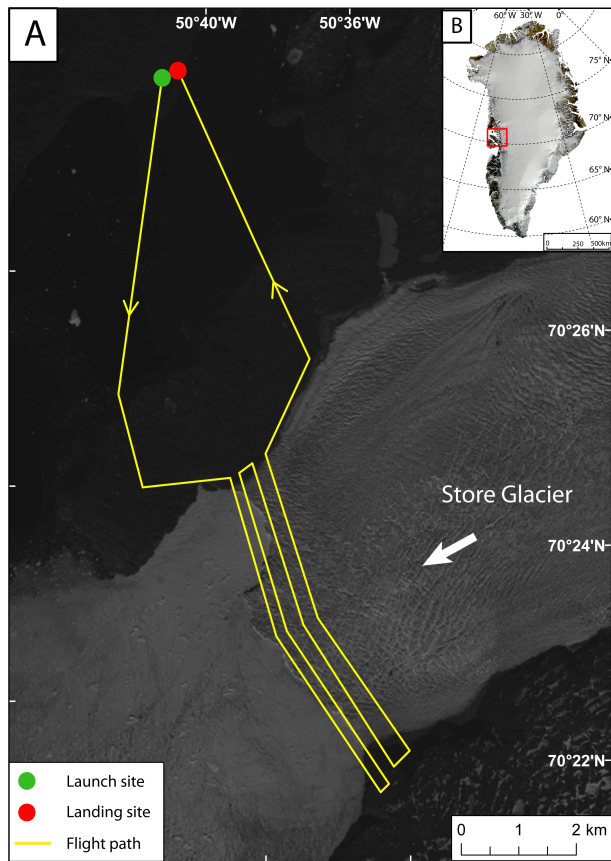
Fig. 1. (A) The planned UAV mission over Store Glacier. The background map is a Landsat 8 panchromatic image from 12 June 2013. The green and red dots show the launching and landing sites and the yellow line shows the planned UAV mission. **(B)** Location of Store Glacier in the Uummannaq Region, West Greenland on a MODIS mosaic image of Greenland (Kargel et al., 2012).

Title Page

Abstract | Introduction

Conclusions | References

Tables | Figures

⏮ | ⏭

◀ | ▶

Back | Close

Full Screen / Esc

Printer-friendly Version

Interactive Discussion
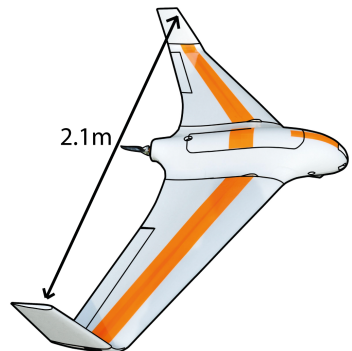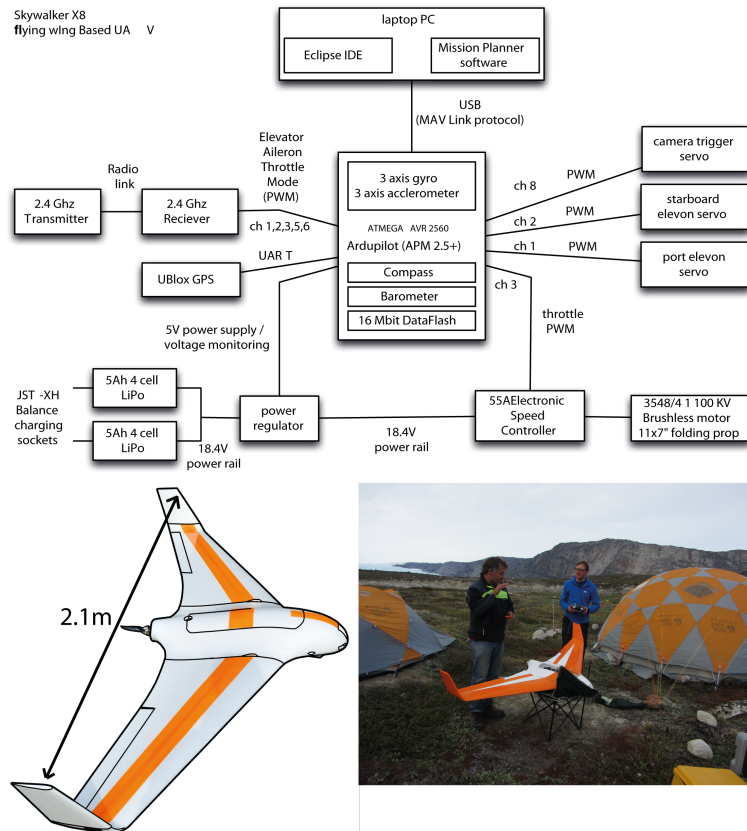
Fig. 2. Flowchart of the control set-up and picture of the UAV at base camp with the "relative novices".
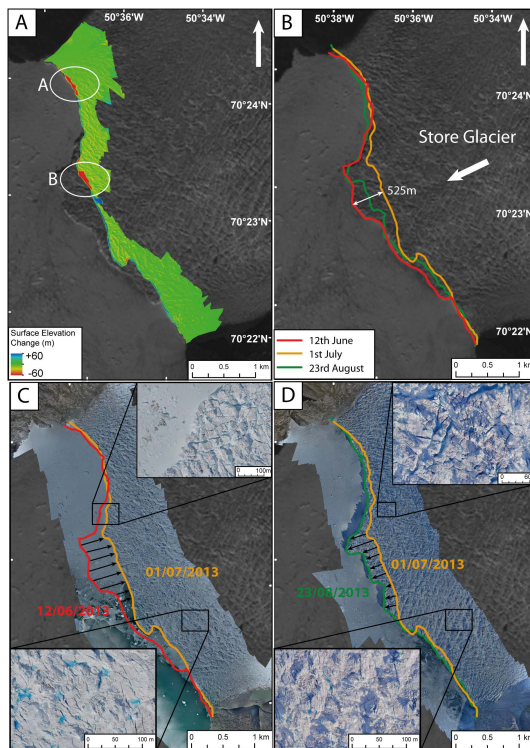
Fig. 3. (A) Surface elevation difference between two DEMs collected on the 1 July and 2 July. Red areas show elevation loss whilst blue areas show elevation gain. White circles highlight the calving events that occurred between the two UAV surveys. **(B)** The position of the calving front of Store Glacier during the summer of 2013. **(C)** Calving front retreat observed between 12 June and 1 July. Inset is an orthorectified image of the water-filled crevasses observed on 1 July with a pixel resolution of 30 cm. **(D)** Calving front advance observed between 1 July and 23 August. Inset is an orthorectified image showing water-filled crevasses observed on 23 August. The coverage and size of water-filled crevasses is smaller.
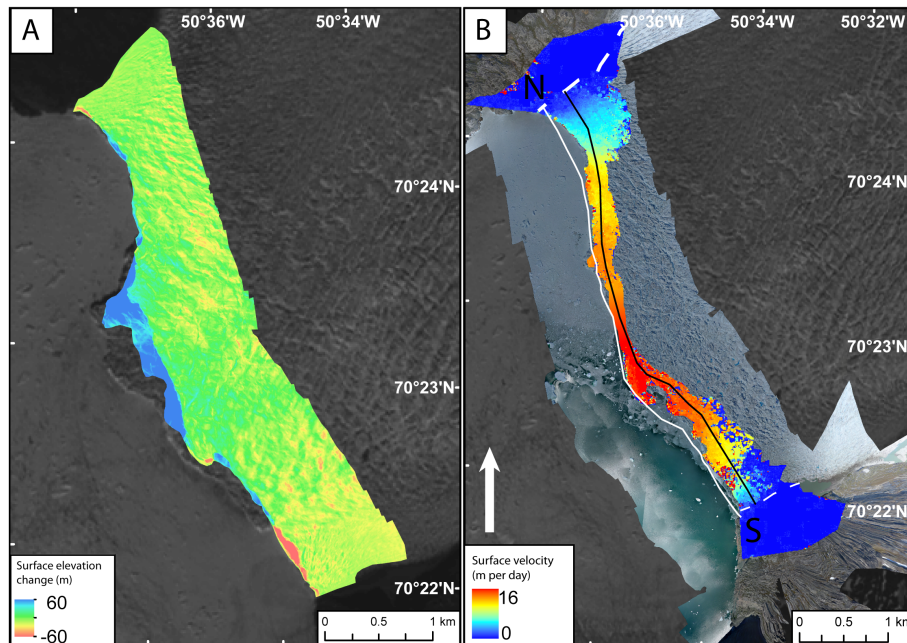
Fig. 4. (A) Surface elevation changes between 2 July and 23 August. An average thinning of $3.5\,\text{m}\,\text{m}^{-1}$ was estimated for the surveyed area. **(B)** The ice flow speed structure of the terminus of Store Glacier between 1 and 2 July 2013. The centre of the glacier flows at approximately $16\,\text{m}\,\text{d}^{-1}$ whilst the margins flow less than $5\,\text{m}\,\text{d}^{-1}$. Dotted white lines show the lateral margins of the glacier. The black line represents the locations of the horizontal velocity and surface elevation values that were used to estimate ice flux. The white line represents the location of the depth values used to estimate ice flux. The cross-section of the calving front derived from these profiles is displayed in Fig. 4a.
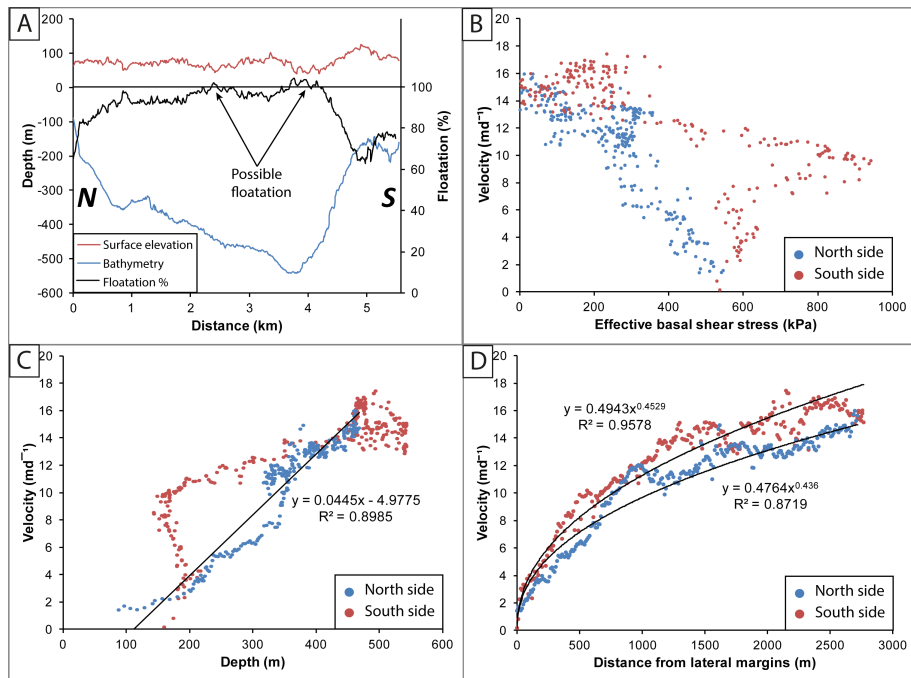
Fig. 5. (A) Profiles showing the sea floor bathymetry and ice surface elevation at the calving front. These data were combined with surface velocities to estimate the ice flux of Store Glacier. Where the floatation percentage is over 100 %, it is assumed that the ice is not thick enough to be fully grounded in hydrostatic equilibrium. **(B)** The relationship between effective basal shear stress and velocity. **(C)** The relationship between depth and velocity. At depths deeper than 400 m, velocities are fairly constant. The two differing relationships between 150 and 350 m represent velocities from different sides of the glacier. **(D)** Relationship between velocity and distance from the lateral margins. The positive correlation demonstrates the importance of the resistance provided by the fjord walls although depth also increases with distance from the fjord walls so can also explain this relationship.
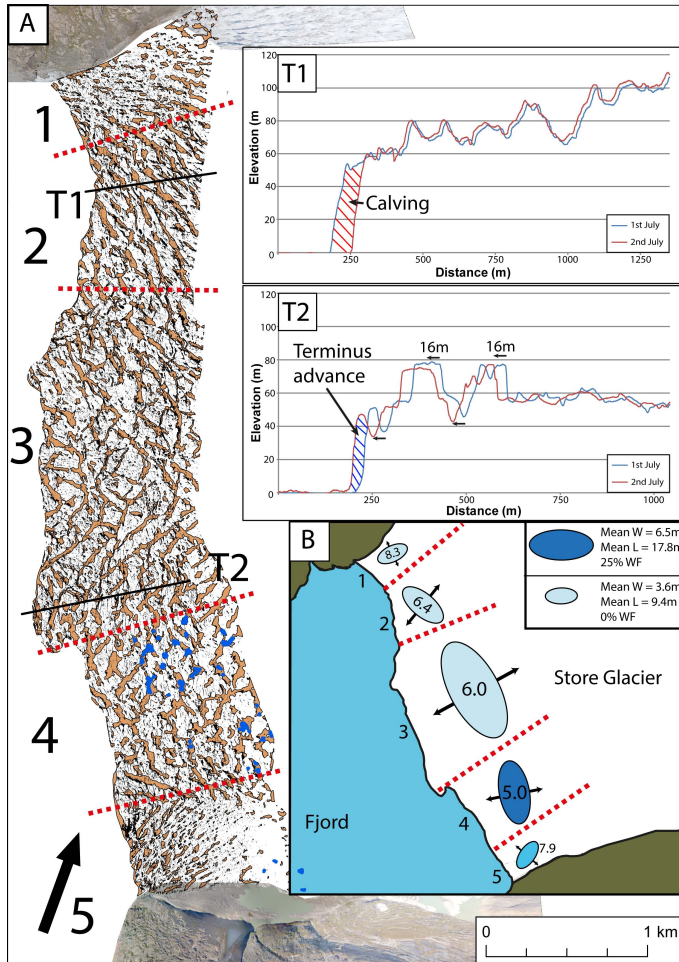
Title Page

Abstract | Introduction

Conclusions | References

Tables | Figures

|◄ | ►|

◄ | ►

Back | Close

Full Screen / Esc

Printer-friendly Version

Interactive Discussion

Fig. 6. (A) Distribution and patterns of crevasses on Store Glacier. Dry crevasses which are large structural features are shown in orange. Narrower crevasses that are observed in the orthorectified images but whose 3-D geometry is not constructed are shown in black. The areas of water-filled crevasses are shown in blue and occur almost exclusively in zone 4. The regions of the terminus that are discussed are designated by the dotted red lines are referred to be the black numbers. Transects 1 and 2 shown in inset demonstrate how crevasses adverted downstream between the 1 and 2 July. In T1, a series of calving events occurred which are discussed as "calving event A". In T2, the calving front advanced 16 m. **(B)** Cartoon of the terminus of Store Glacier with ellipsoids proportional to the average length, width and orientation of crevasses shown in **(A)** for the respective zones. The colour of the ellipsoids represents the proportion of crevasses that are water-filled in each zone where WF refers to water-filled in the legend. The italicized numbers denote the density of crevasses per $10\,\text{m}^2$ in each zone. Arrows illustrate inferred direction of principal strain.

Title Page

Abstract | Introduction

Conclusions | References

Tables | Figures

⏮ | ⏭

◀ | ▶

Back | Close

Full Screen / Esc

Printer-friendly Version

Interactive Discussion